processes

MDPI

Article

Three-Dimensional Study of Contact Melting of a Molten Material Crust Against a Stainless Steel Plate During a Severe Reactor Accident

Junjie Ma, Yuqing Chen, Wenzhen Chen * and Hongguang Xiao

Naval University of Engineering, Wuhan 430033, China; 19500401@nue.edu.cn (J.M.)
* Correspondence: Cwz2@21cn.com

Abstract

In severe reactor accidents, molten corium solidifies within the core to form a corium crust. Under decay heat, the high-temperature corium crust induces contact melting of internal reactor components. Given the narrow and limited dimensions of these components, this study investigated the contact melting of a corium crust against a stainless steel plate. A three-dimensional plate contact melting model for plate-shaped corium is proposed, with its validity demonstrated through experimental verification. The patterns and factors influencing contact melting were analyzed. The results indicate that under constant heat flux boundary conditions, the melting rate depends solely on the magnitude of the heat flux density, while the effects of the contact surface geometry and heat source mass on the melting rate are negligible. The thickness of the molten liquid film is proportional to both the heat flux density and contact surface area, yet inversely proportional to both the heat source mass and aspect ratio of the contact surface. When the aspect ratio exceeds six, the model can be simplified to two dimensions.

Keywords: contact melting; severe accident; core melting; plate



Academic Editor: João Duarte Neves Cruz

Received: 11 September 2025
Revised: 8 October 2025
Accepted: 10 October 2025
Published: 16 October 2025

Citation: Ma, J.; Chen, Y.; Chen, W.; Xiao, H. Three-Dimensional Study of Contact Melting of a Molten Material Crust Against a Stainless Steel Plate During a Severe Reactor Accident. *Processes* **2025**, *13*, 3310. https://doi.org/10.3390/pr13103310

Copyright: © 2025 by the authors. Licensee MDPI, Basel, Switzerland. This article is an open access article distributed under the terms and conditions of the Creative Commons Attribution (CC BY) license (https://creativecommons.org/licenses/by/4.0/).

1. Introduction

Following the nuclear accidents at Three Mile Island in the United States in 1979, Chernobyl in the former Soviet Union in 1986, and particularly the Fukushima accident in Japan in 2011, it was recognized that severe nuclear accidents pose profound and far-reaching hazards and consequences. Thus, severe accidents and related issues have become a major focus in the field of nuclear safety research [1]. As demonstrated by the Three Mile Island accident [2], during the core melting process, relocated molten material may solidify and form a molten pool. As the pool expands, the surface crust of the molten pool may mechanically interact with internal structures (such as support plates, core shrouds, reactor vessel baffles, and other supporting components), leading to contact melting [3]. Under severe accident conditions, the melting of support structures constitutes the primary source of the metallic layer in the lower head molten pool. The progression of their melting affects the thickness of this metallic layer [4,5]. The metallic layer induces a heat concentration effect on the lower head wall, thereby threatening the integrity of the reactor pressure vessel. Furthermore, in the case of dispersion fuel element reactor types, the low melting point of their fuel support matrix means that the high-temperature solidified crust can cause melting of the underlying fuel elements supporting it. These two aspects will thereby increase the uncertainty in the melt progression during severe core accidents. While the melt behavior

of the core can currently be effectively assessed using system-level codes [6], it remains challenging to accurately simulate the melting process of specific internal components or perform mechanistic analysis of their melting behavior [7]. Regarding research on the melting behavior of internal reactor components, the current theoretical models primarily include radiation heat transfer models and melting–solidification models [8], which are fundamentally non-contact melting models. However, the melting interaction between the corium crust and internal structures is a typical contact melting process. According to existing studies, contact melting can achieve a melting rate one to seven times higher than that of stationary melting under identical operational conditions [9], significantly accelerating the core melt progression.

Contact melting refers to the phenomenon that occurs when a solid phase-change material is pressed against a heat source whose temperature exceeds the melting point of the phase-change material. It is currently widely applied in multiple fields such as energy storage, welding, geological exploration, and nuclear technology [10]. Scholars including Emerman [11], Moallemi [12], and Chen [13] have conducted studies on relevant contact melting models within the context of core melting, demonstrating the feasibility of applying this theory to nuclear-related issues. For contact melting processes involving moving heat sources, analytical models have been established for two-dimensional contact melting around heat sources with various geometries, including cylinders [14–16], spheres [17], ellipsoidal cylinders [18], and parabolic cylinders [19]. However, for internal reactor components, their dimensions are generally smaller than those of the core melt pool and simplifications to two-dimensional models may introduce deviations. Additionally, given the dynamic nature of severe accidents in reactors, the applicability of governing equations for contact melting under different thermal boundary conditions remains unclear and requires further analysis.

Due to the complex geometry of corium, this study adopts a simplified representation for the external morphology of the corium crust. Based on observations from the Three Mile Island accident, the corium crust typically forms a bowl-shaped structure [20]. In this configuration, the central region of the corium crust exhibits relatively flat geometry, allowing its contact interface with the underlying stainless steel components to be approximated as horizontal. Consequently, a plate-like structure is employed to simulate the shape of the corium crust. Following reactor shutdown in a severe accident, a significant amount of decay heat continues to be generated. The thermal power declines rapidly within a relatively short period before transitioning to a more gradual decrease [21]. According to research by Hong et al. [22], the melting velocity experiences a brief increase (on the order of approximately 10^{-6} s) after the initiation of contact melting before stabilizing at a quasi-steady level. Consequently, the melting process can be analyzed using a quasi-steady-state approach at each time step. This study employs a constant heat flux boundary condition to model the thermal characteristics at the surface of the corium crust. The rationality of the derived model was validated through experimental investigations, followed by a comprehensive sensitivity analysis of key parameters. Ultimately, governing equations applicable to contact melting phenomena under severe reactor accident conditions were established.

2. Physical Model

2.1. Geometric Configuration

Figure 1 presents a schematic diagram of the contact melting model between a horizontal heated plate and a three-dimensional stainless steel plate. The heat source plate has dimensions of length 2A, width 2B, and height C. A molten stainless steel specimen is positioned centrally beneath the heated plate, with its contact surface di-

mensions being 2a × 2b (where A > a, B > b). Under gravitational force, the heated plate exerts compressive stress and induces melting of the underlying stainless steel specimen. The coordinate system is defined with the *z*-axis normal to the contact surface, the *x*-axis aligned with the dimension a (length direction), and the *y*-axis aligned with the dimension b (width direction). The origin of the coordinate system is located at the center of the contact surface.

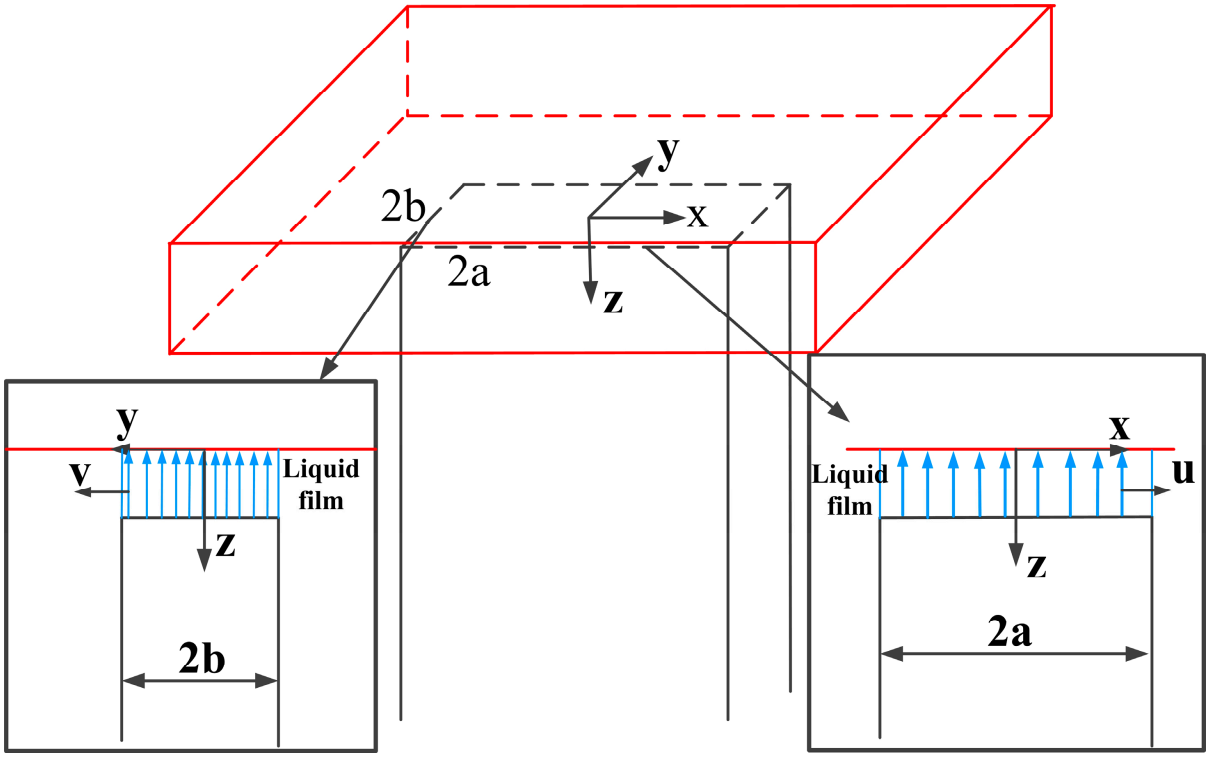


Figure 1. Three-dimensional plate contact melting model.

2.2. Theoretical Methodology

Based on the characteristics of contact melting and relevant findings [23,24], the following assumptions are adopted for the aforementioned melting process:

1. The solid–liquid phase interface remains distinct, and the process is considered quasi-steady;
2. The flow within the molten liquid film is laminar, with the liquid behaving as a Newtonian fluid whose thermophysical properties are treated as constant;
3. The liquid film is extremely thin, and the flow is dominated by viscous forces. Consequently, inertial terms in the momentum equations are negligible, reducing the balance to that between the pressure gradient and viscous shear forces.

Based on the aforementioned assumptions, the governing equations for the liquid film are given by the mass conservation, momentum conservation, and energy conservation as follows:

$$\frac{\partial u}{\partial x} + \frac{\partial v}{\partial y} + \frac{\partial w}{\partial z} = 0 \tag{1}$$

$$\frac{\partial P(x,y)}{\partial x} = \mu \frac{\partial^2 u}{\partial z^2} \tag{2}$$

$$\frac{\partial P(x,y)}{\partial y} = \mu \frac{\partial^2 v}{\partial z^2} \tag{3}$$

$$\alpha \frac{\partial^2 T}{\partial z^2} = u\frac{\partial T}{\partial x} + v\frac{\partial T}{\partial y} + w\frac{\partial T}{\partial z} \tag{4}$$

where u, v, and w represent the velocity components of the liquid within the film along the x, y, and z-axes, respectively; P denotes the pressure in the liquid film; μ is the dynamic viscosity coefficient of the liquid; and α represents the thermal diffusivity of the liquid, defined as $\alpha = \lambda/\rho c_p$, where λ is the thermal conductivity, ρ is the density, and c_p is the specific heat capacity of the liquid.

The boundary conditions for the liquid film are specified as follows:

$$\text{When } z = 0,\ u = v = 0,\ w = U \tag{5}$$

$$\text{When } z = \delta,\ u = v = w = 0, \tag{6}$$

where δ denotes the thickness of the liquid film and U represents the downward melting velocity of the heated plate.

Based on boundary conditions (5) and (6), the governing Equations (2) and (3) can be solved as follows:

$$u = \frac{1}{2\mu}\frac{dP}{dx}(z^2 - \delta z) \tag{7}$$

$$v = \frac{1}{2\mu}\frac{dP}{dy}(z^2 - \delta z) \tag{8}$$

Substituting Equations (7) and (8) into the continuity Equation (1) and simplifying yields the following expression:

$$\frac{1}{2\mu}\frac{\partial^2 P}{\partial x^2}(z^2 - \delta z) + \frac{1}{2\mu}\frac{\partial^2 P}{\partial y^2}(z^2 - \delta z) + \frac{\partial w}{\partial z} = 0 \tag{9}$$

Integrating the above equation with respect to z from 0 to δ and applying boundary conditions (5) and (6) yields the following result:

$$\frac{\partial^2 P}{\partial x^2} + \frac{\partial^2 P}{\partial y^2} = S \tag{10}$$

where $S = -\frac{12\mu U}{\delta^3}$.

For the liquid film, the boundary condition is given by P(±a, y) = P(x, ±b) = 0.

To solve for P(x, y), the method of particular solutions [25] can be employed by decomposing it into the following form:

$$P(x, y) = P_1(x) + P_2(x, y) \tag{11}$$

Substituting Equation (11) into Equation (10), the original governing equations can be decomposed into the following two equations:

$$\frac{d^2 P_1}{dx^2} = S, P_1(\pm a) = 0 \tag{12}$$

$$\frac{d^2 P_2}{dx^2} + \frac{d^2 P_2}{dy^2} = 0, P(\pm a, y) = 0, P(x, \pm b) = -P_1(x) \tag{13}$$

Equation (12) can be solved to yield the following:

$$P_1(x) = \frac{S}{2}(x^2 - a^2) \tag{14}$$

For $P_2(x, y)$, the solution can be obtained via the separation of variables method with reference to [26], yielding the following:

$$P_2(x,y) = \sum_{n=1}^{\infty} \frac{16Sa^2(-1)^{n+1}}{(2n-1)^3\pi^3\cosh(\frac{(2n-1)\pi b}{2a})} \cos(\frac{(2n-1)\pi x}{2a}) \cosh(\frac{(2n-1)\pi y}{2a}) \quad (15)$$

By combining Equations (14) and (15), the solution can be obtained as follows:

$$P(x,y) = \frac{S}{2}(x^2-a^2) + \sum_{n=1}^{\infty} \frac{16Sa^2(-1)^{n+1}}{(2n-1)^3\pi^3\cosh(\frac{(2n-1)\pi b}{2a})} \cos(\frac{(2n-1)\pi x}{2a}) \cosh(\frac{(2n-1)\pi y}{2a}) \quad (16)$$

Based on the force balance relationship of the heat source under quasi-steady-state conditions, we obtain the following:

$$M_h g = \int_{-a}^{a}\int_{-b}^{b} P(x,y)dxdy \quad (17)$$

where M_h represents the mass of the heat source.

Substituting Equation (16) into Equation (17) yields the following:

$$M_h g = -\frac{4a^3b}{3}S + \frac{256Sa^4}{\pi^5}\sum_{n=1}^{\infty}\frac{\tanh(\frac{(2n-1)\pi b}{2a})}{(2n-1)^5} \quad (18)$$

By combining the expression for S and simplifying Equation (18), the expression for the velocity U can be derived as follows:

$$U = \frac{M_h g\delta^3}{16a^3b\mu(1-\frac{192a}{\pi^5 b}\sum_{n=1}^{\infty}\frac{\tanh(\frac{(2n-1)\pi b}{2a})}{(2n-1)^5})} \quad (19)$$

Due to the extreme thinness of the liquid film ($\delta << a$, $\delta << b$), the temperature gradient in the vertical direction can be considered significantly greater than that in the horizontal directions. Thus, Equation (4) can be simplified to the following:

$$\alpha\frac{\partial^2 T}{\partial z^2} = w\frac{\partial T}{\partial z} \quad (20)$$

Integrating Equation (9) with respect to z from 0 to z yields the liquid film temperature distribution as follows:

$$w(z) = U - (\frac{1}{3}z^3 - \frac{\delta}{2}z^2)(\frac{\partial^2 P}{\partial x^2} + \frac{\partial^2 P}{\partial y^2})\frac{1}{2\mu} \quad (21)$$

By combining Equation (10) with Equation (21), the following relationship can be obtained:

$$w(z) = U[1 + (2\frac{z}{\delta^3}^3 - 3\frac{z}{\delta^2}^2)] \quad (22)$$

Under the boundary condition of the second kind (Neumann boundary condition), the thermal behavior is characterized by the following equation:

$$-\lambda\frac{\partial T}{\partial z}\Big|_{z=0} = q'' \quad (23)$$

By combining Equations (20), (22) and (23), the expression for the temperature gradient dT/dz can be derived as follows:

$$\frac{\mathrm{d}T}{dz} = -\frac{q''}{\lambda} e^{\frac{U}{\alpha}\left[z+\frac{1}{2}\frac{z^4}{\delta^3}-\frac{z^3}{\delta^2}\right]} \tag{24}$$

Under actual severe reactor accident conditions, the axial temperature gradient within the phase-change material (stainless steel) results in only a portion of the heat flux entering the solid–liquid interface being utilized for melting. Therefore, the heat transfer at this interface must account for two components: first, the latent heat of phase change, and second, the heat conduction within the stainless steel phase-change material. Accordingly, the energy conservation condition at the solid-liquid interface (z = δ) can be expressed as follows:

$$-\lambda \frac{\partial T}{\partial z}\bigg|_{z=\delta^+} - (-\lambda \frac{\partial T}{\partial z}_{|z=\delta^-}) = -\rho_{\mathrm{m}} U L_m \tag{25}$$

where $-\lambda \frac{\partial T}{\partial z}_{|z=\delta^-}$ represents the heat flux density transferred toward the phase-change material side, denoted as q_s'', whose value must be determined based on the temperature gradient within the phase change material.

By combining Equations (24) and (25), the following expression can be derived:

$$\delta = -\frac{2\alpha \ln(\frac{\rho_m U L_m + q''_s}{q''})}{U} \tag{26}$$

From Equations (19) and (26), the contact melting equation for a horizontal heated plate source against a stainless steel plate under a constant heat flux density condition can be derived as follows:

$$\begin{cases} \delta = -\dfrac{2\alpha \ln(\dfrac{\rho_m U L_m + q''_s}{q''})}{U} \\ U = \dfrac{M_h g \delta^3}{16 a^3 b \mu (1 - \dfrac{192a}{\pi^5 b} \sum\limits_{n=1}^{\infty} \dfrac{\tanh(\dfrac{(2n-1)\pi b}{2a})}{(2n-1)^5})} \end{cases} \tag{27}$$

Since Equation (27) contains an infinite series expansion term along with implicit integral and logarithmic terms, it is difficult to obtain explicit expressions for the melting velocity U and the liquid film thickness δ through analytical methods. Therefore, this study employs a numerical iteration approach, considering the solution converged when the absolute iteration error falls below 1×10^{-3}.

3. Experimental Validation

To validate the correctness of the derived governing equations, this study conducted contact melting experiments involving a flat-plate heat source and a single stainless steel plate. The validation was performed by comparing the experimental results with the predicted melting velocity. Given the prohibitively high cost of conducting contact melting experiments with stainless steel due to its extremely high melting point, and considering that the governing Equation (27) established in this work incorporates key thermophysical parameters such as thermal diffusivity (α) and dynamic viscosity (μ), the model is inherently universal and not restricted to any specific phase-change material. Therefore, employing a low-melting-point material for experimental validation not only significantly

simplifies the setup and reduces costs but also effectively verifies the predictive accuracy and general applicability of the governing equation for the contact melting process.

Figure 2 shows a schematic diagram of the experimental setup. The yellow metal indicated by the red arrow represents the heat source plate, while the silver metal indicated by the yellow arrow below corresponds to the plate-shaped phase-change material specimen. The heat source plate is made of copper and is equipped with embedded heating resistors wound around its interior to provide thermal power. Five temperature measurement points are uniformly distributed on the upper surface of the heat source to monitor the temperature variation of the copper plate. The phase-change material for melting is a tin block with dimensions of 3 cm × 2 cm × 10 cm, positioned directly beneath the copper heat source plate. The melting phase-change material is fixed on the workbench, aligned with the central axis of the heat source plate.

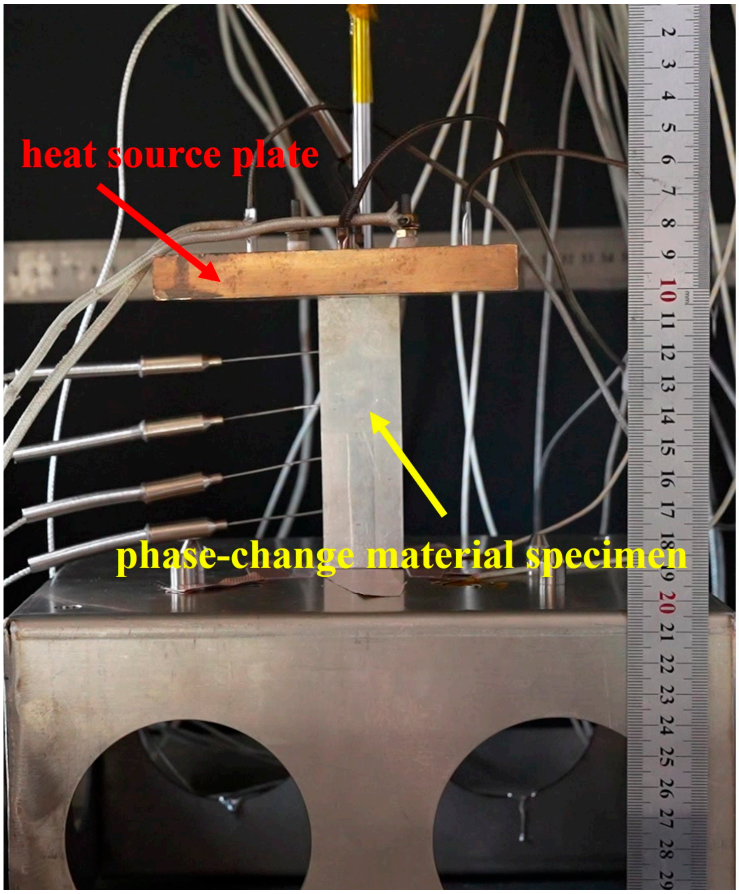


Figure 2. Schematic diagram of the contact melting experiment.

At the beginning of the experiment, a constant power of 300 W was applied to the copper heat source plate. After melting initiated, the downward melting distance h_m was recorded every 10 s. The melting velocity was determined by differentiating h_m using the central difference method. At five specific time points during the melting process, the heat flux q'' transferred from the heat source to the phase-change material was calculated based on temperature variations measured by the thermocouples on the heat source and the principle of energy conservation. Simultaneously, the heat flux q_s'' transferred toward the phase-change material side at the melting interface was derived using temperature measurements at various heights of the phase-change material and the displacement of the contact surface. By substituting the obtained q'' and q_s'' into Equation (27), along with the thermophysical properties of the experimental materials, the theoretical melting velocity was calculated.

The uncertainty in the melting velocity primarily originates from the reading of the melting distance h_m. Based on an experimental uncertainty analysis, the uncertainty in the melting velocity is estimated to be 2×10^{-5} m/s. A comparison between the experimental and theoretical values of the melting velocity is shown in Figure 3. As can be seen from the figure, the average error between the theoretical and experimental values is 6.8%, with a maximum error of 11%. The observed discrepancies primarily stem from two factors: firstly, fluctuations in data acquisition during melting velocity measurements due to the small melting distance; and secondly, systematic errors in the temperature data collection system. Nevertheless, the overall trends of the theoretical and experimental results show good agreement, demonstrating the rationality of the derived model and confirming the quasi-steady-state characteristics of the contact melting process.

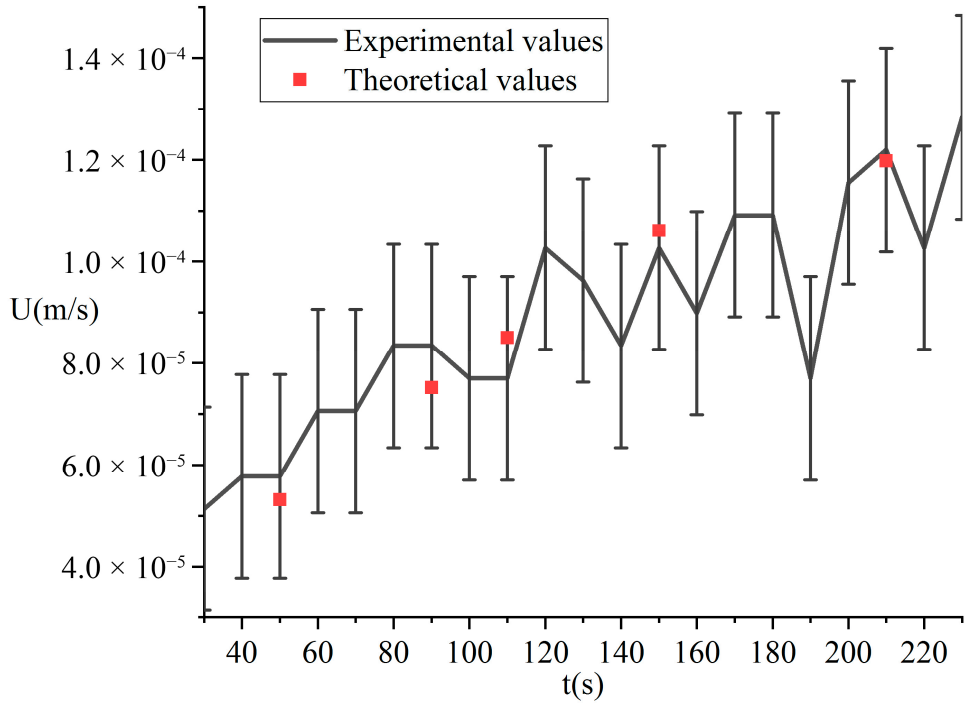


Figure 3. Comparison of theoretical and experimental values.

4. Analysis and Discussion

To facilitate analysis, this study adopts the AP1000 reactor thermal power as a reference to normalize the heat flux q'', where q''_{max} represents the full-power heat flux of the AP1000. Assuming a core meltdown accident occurs one hour after reactor shutdown in a severe accident, the decay heat power at this point is approximately 1% of the rated full power. However, the formation of a molten pool through the accumulation of corium crust can lead to a significant increase in heat flux in localized regions. To account for this concentration effect and cover more severe scenarios, this study conservatively assumes a maximum local heat flux of up to 5% of the full-power heat flux [27]. To closely represent internal reactor components, 1Cr18Ni9Ti stainless steel is selected as the phase-change material for analysis, with its thermophysical properties listed in Table 1 [19].

Table 1. The physical parameters of the 1Cr18Ni9Ti type stainless steel [19].

ρ_f (kg/m³)	λ_f (W/m·K)	c_{pf} (J/(kg·K))	L_m (J/kg)	μ_f (kg/(m·s))	T_m (K)
7900	26.8	580	2.72×10^5	5.9×10^{-3}	1700

Figures 4 and 5, respectively, illustrate the variations of melting velocity and liquid film thickness with heat flux for a melting specimen of dimensions a = 0.2 m and b = 0.05 m under different heat source masses. Under the Neumann boundary condition, the melting velocity exhibits an approximately linear increase with rising heat flux, as shown in Figure 4. Notably, the influence of heat source gravity variation on the melting velocity is extremely marginal, inducing differences of less than 0.002%. This indicates that the effect of heat source gravity on the melting rate is negligible, a conclusion consistent with experimental observations reported in previous studies [28].

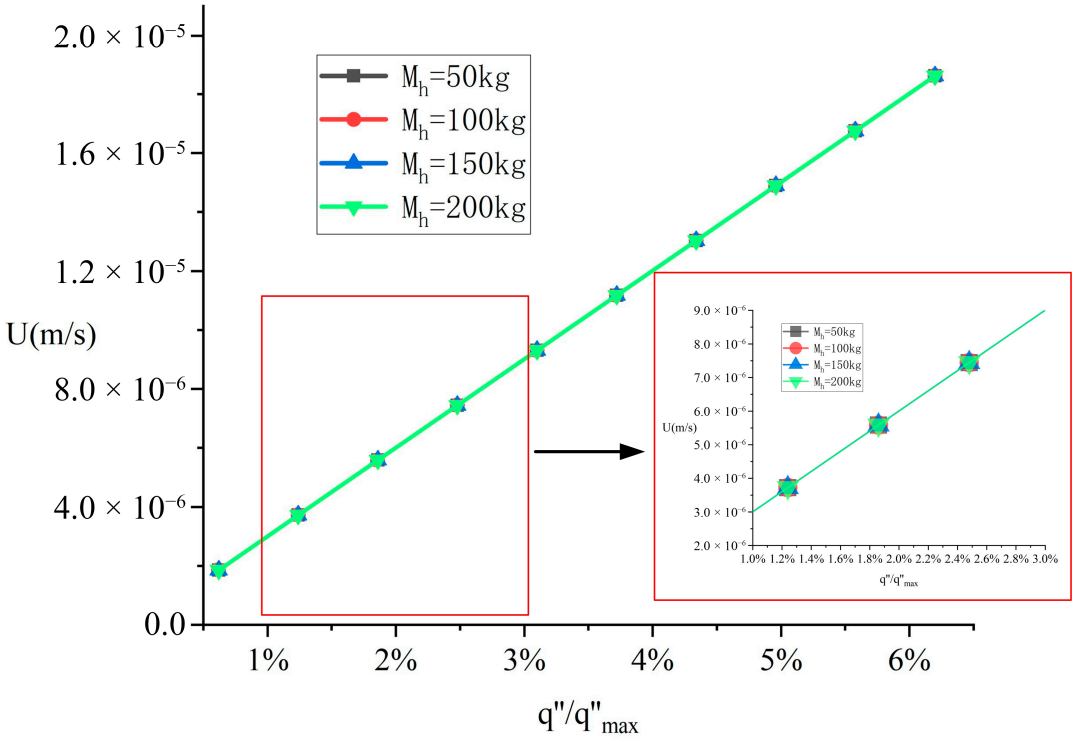


Figure 4. Variation of melting velocity with heat flux.

Figure 5 demonstrates the correlation between heat flux and liquid film thickness. As the heat flux increases, the liquid film thickness exhibits a monotonically increasing trend. Moreover, greater heat source gravity results in reduced liquid film thickness. This phenomenon can be explained by the liquid film pressure relationship in Equation (16): the liquid film pressure P is inversely proportional to the film thickness δ. When the gravity of the heating body increases, a higher liquid film pressure is required to maintain the force equilibrium of the film, leading to a corresponding reduction in film thickness. Furthermore, by comparing liquid film thicknesses under identical heat flux but different heat source masses, it can be observed that the influence of the heat source mass on film thickness gradually diminishes as the mass increases.

The contact area S_c and aspect ratio of the phase-change material ξ are key factors influencing the contact melting process. To independently analyze the respective mechanisms of these two parameters, this study employs a control variable approach: when examining the effect of contact area, the aspect ratio is maintained at four while varying the dimensions to alter the contact area; when investigating the impact of aspect ratio, the contact area is held constant while adjusting the side length proportions to modify the aspect ratio. Given the equivalent influence of the aspect ratio definition on parametric effects, and to simplify the presentation, the analysis assumes a < b during the aspect ratio investigation.

Figures 6 and 7 illustrate the influence of different aspect ratios on the contact melting process while maintaining a constant contact area of 4 cm^2. As shown in Figure 6, the effect of aspect ratio on melting velocity is negligible. However, the liquid film thickness decreases significantly with increasing aspect ratio, as demonstrated in Figure 7.

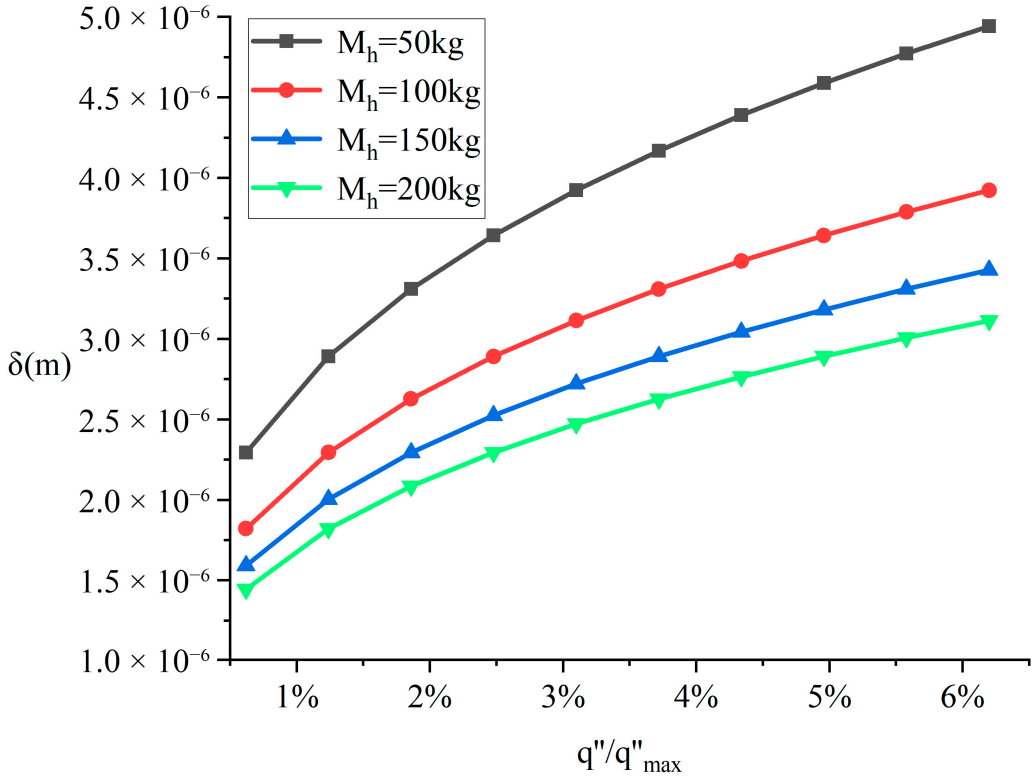


Figure 5. Variation of liquid film thickness with heat flux.

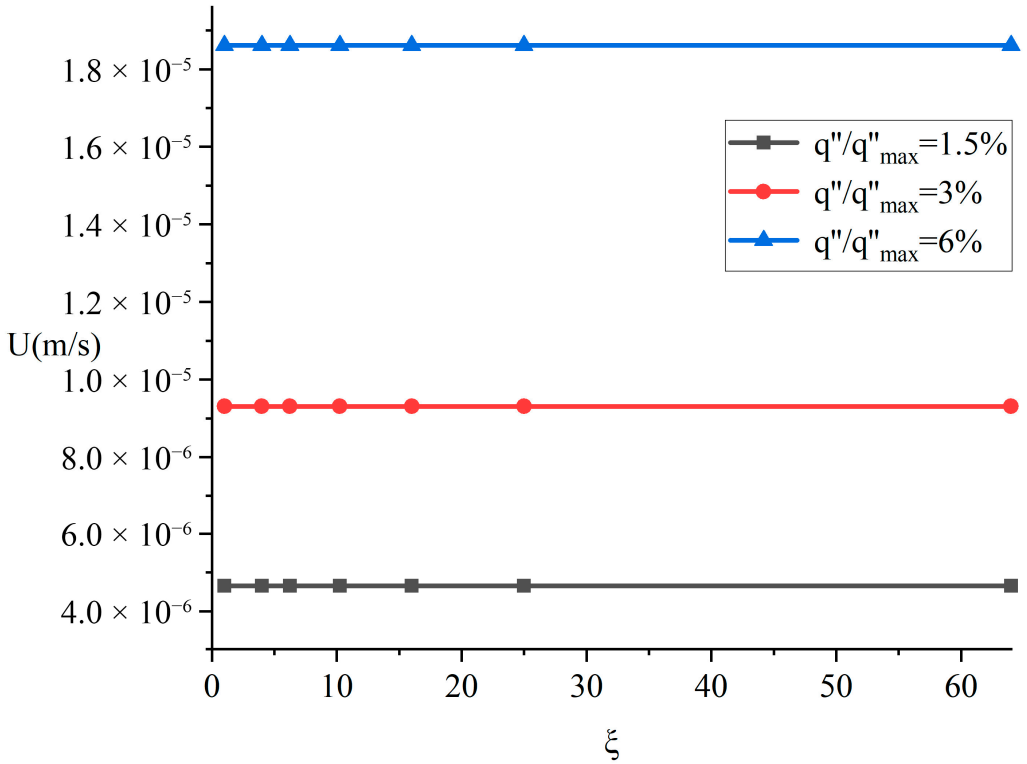


Figure 6. Variation of melting velocity with aspect ratio.

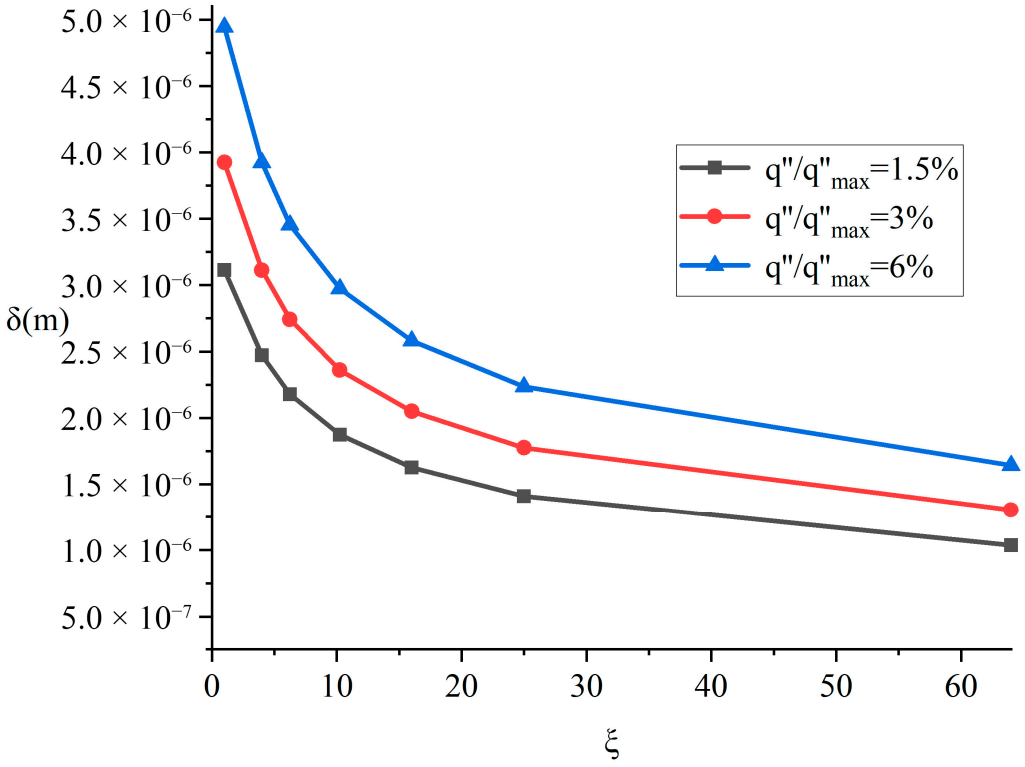


Figure 7. Variation of liquid film thickness with aspect ratio.

When the contact area remains constant, an increase in the aspect ratio implies a reduction in the dimension of the contact surface along one specific direction. This facilitates easier drainage of molten liquid from the shorter edges. Since the melting velocity remains largely unchanged, the total volume of molten liquid generated per unit time is constant. Consequently, more liquid flows out along the narrower side with smaller dimensions, leading to an increased flow velocity in this region. This significantly enhances the local convective heat transfer intensity. The intensified heat transfer reduces the temperature of the heat source contact surface. To maintain the constant heat flux boundary condition, the liquid film thickness must correspondingly decrease.

Figures 8 and 9 illustrate the variations of melting velocity and liquid film thickness with contact area under different heat flux conditions, while maintaining a fixed aspect ratio of four and a constant heat source mass of 100 kg. As observed in Figure 8, the influence of contact area on melting velocity is minimal and essentially negligible. Figure 9 demonstrates a proportional relationship between the contact area and liquid film thickness. Under the condition of constant total heat source mass, an increase in contact area leads to a reduction in the unit area pressure acting on the liquid film. According to Equation (16), which states that pressure is inversely proportional to liquid film thickness, this decrease in pressure results in an increase in film thickness.

Existing severe accident analysis codes predominantly employ one-dimensional or two-dimensional models to reduce computational complexity. However, such dimensional simplifications may significantly impact the predictive accuracy of key physical processes. It is therefore essential to evaluate the applicability of dimensional reduction in modeling contact melting phenomena involving internal reactor components.

The two-dimensional (2D) model is formulated based on the geometric condition where the material's width a (in the x direction) is considerably smaller than its length b (in the y direction). Under this assumption, the system can be considered infinite in the y direction, allowing us to neglect flow and gradients along that axis. Consequently, the

contact melting problem is simplified to be governed by the equations solved within the x–z plane only.

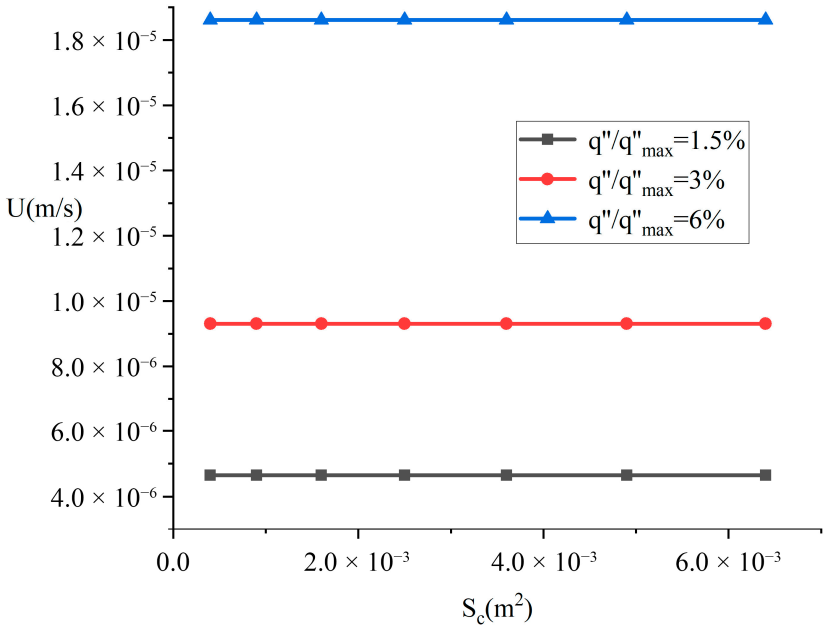


Figure 8. Variation of melting velocity with contact area.

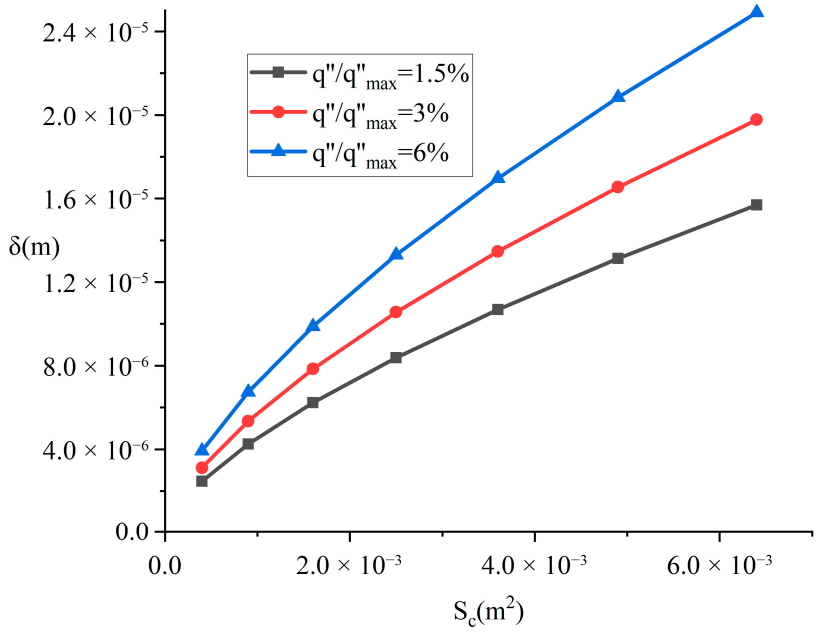


Figure 9. Variation of liquid film thickness with contact area.

When $a << b$, the condition $\frac{\partial P}{\partial a} >> \frac{\partial P}{\partial b}$ holds. According to Equations (7) and (8), this results in $u >> v$, allowing the neglect of molten liquid flow in the y direction and reducing the governing equations for the liquid film to a two-dimensional flow formulation. Under this condition, Equation (10) simplifies to:

$$\frac{\partial^2 P}{\partial x^2} = -\frac{12\mu U}{\delta^3} \tag{28}$$

For the above equation, the solution is obtained using the boundary condition P(±a) = 0:

$$\mathrm{P} = -\frac{6\mu U}{\delta^3}(x^2 - a^2) \tag{29}$$

Based on the force balance relationship under quasi-steady-state conditions, the following equation is given:

$$M_h g = 2b\int_{-a}^{a} P(x)dx \tag{30}$$

By combining Equations (29) and (30), the solution can be derived as follows:

$$\mathrm{U} = \frac{M_h g \delta^3}{16\mu a^3 \mathrm{b}} \tag{31}$$

By combining Equations (30) and (31), the governing equation for contact melting under the two-dimensional model can be derived as follows:

$$\begin{cases} \delta = -\frac{2\alpha \ln(\frac{\rho_m U L_m + q_s}{q''})}{U} \\ U = \frac{M_h g \delta^3}{16 a^3 b \mu} \end{cases} \tag{32}$$

By comparing Equation (32) with Equation (27), it can be observed that the difference between the two-dimensional and three-dimensional models lies in a correction factor:

$$(1 - \frac{192}{\pi^5 \xi}\sum_{n=1}^{\infty}\frac{\tanh(\frac{(2n-1)\pi\xi}{2})}{(2n-1)^5}) \tag{33}$$

This factor is inherently geometry-dependent, indicating that the two-dimensional model neglects liquid flow in the y direction (lateral direction) and assumes all molten liquid flows exclusively along the x direction. Given that the influence of the aspect ratio on the melting front propagation velocity is negligible, and its primary effect manifests in the liquid film thickness, a systematic analysis of the deviation between the liquid film thickness predicted by the two-dimensional model and the three-dimensional benchmark values is conducted here to quantitatively assess the simplification error of the two-dimensional model.

Figure 10 presents the variation of liquid film thickness and its relative error with aspect ratio, calculated by both two-dimensional and three-dimensional contact melting models under the conditions of M_h = 100 kg, q''/q''_{max} = 4%, and a contact area of 4 cm^2. The left vertical axis represents the liquid film thickness, while the right vertical axis indicates the relative error coefficient. Analysis of Figure 10 indicates that when the aspect ratio is one, the discrepancy between the liquid film thickness values calculated by the three-dimensional and two-dimensional models is most significant, with an error as high as 33.4%. As the aspect ratio increases, the error decreases rapidly, dropping to 4% at an aspect ratio of six. This significant error trend reveals the critical influence of aspect ratio on the direction of liquid outflow. For square contact surfaces, the two-dimensional model systematically overestimates the liquid film thickness, resulting in a predicted liquid outflow velocity along the short axis (x-axis) that is higher than the actual value. This implies that in the two-dimensional model, the required temperature of the heat source contact surface to achieve the same melting state is underestimated, ultimately leading to a predicted slower melting progression. It is particularly noteworthy that when the aspect ratio is less than three, the relative error of the two-dimensional model

increases significantly. In such cases, a three-dimensional model must be employed for contact melting analysis.

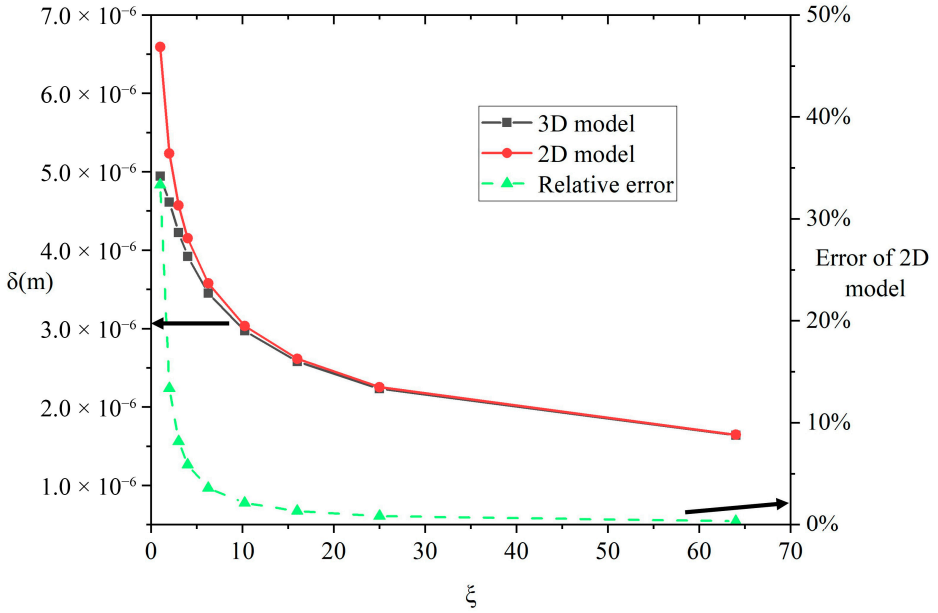


Figure 10. Comparison of 2D and 3D model predictions for liquid film thickness and computational error versus aspect ratio (M_h = 100 kg, q''/q''_{max} = 4%, Sc = 4 cm^2).

To compare the effects of thermal boundary conditions on contact melting, the following section derives the contact melting equations for a horizontal plate heat source interacting with a three-dimensional plate-shaped phase change material under the Dirichlet boundary condition.

The boundary condition expressed in Equation (23) is modified as follows:

$$z = 0, T = T_w \qquad z = \delta, T = T_m \tag{34}$$

By combining Equations (20), (22), and (34), the expression for the temperature gradient can be derived as follows:

$$\frac{\partial T}{\partial z} = \frac{(T_w - T_m)e^{(\frac{U}{\alpha}(z+\frac{z^4}{2\delta^3}-\frac{z^3}{\delta^2}))}}{\int_0^\delta e^{(\frac{U}{\alpha}(z+\frac{z^4}{2\delta^3}-\frac{z^3}{\delta^2}))}dz} \tag{35}$$

By incorporating the melting energy relationship at the phase-change material surface expressed in Equation (25), the expressions for the velocity U and the liquid film thickness δ under the first-kind boundary condition (Dirichlet boundary condition) can be derived as follows:

$$\begin{cases} \dfrac{(T_m - T_w)e^{(\frac{U\delta}{2\alpha})}}{\int_0^\delta e^{(\frac{U}{\alpha}(z+\frac{z^4}{2\delta^3}-\frac{z^3}{\delta^2}))}dz} = -\dfrac{\rho_m U L_m + q''_s}{\lambda} \\ U = \dfrac{M_h g \delta^3}{16a^3 b\mu(1 - \frac{192a}{\pi^5 b}\sum_{n=1}^{\infty}\frac{\tanh(\frac{(2n-1)\pi b}{2a})}{(2n-1)^5})} \end{cases} \tag{36}$$

Based on Equation (36), the influence of various parameters on the melting process under the Dirichlet boundary condition can be analyzed. This section focuses on the heat source mass as an example to examine its specific effects.

To enable a direct comparison between the Dirichlet boundary condition and Neumann boundary condition, the wall temperature T_w for the Dirichlet boundary condition was determined based on the melting parameters obtained from Figure 4 for M = 100 kg. The heat conduction within the liquid film is defined by Equation (37):

$$q'' = \lambda \frac{T_w - T_m}{\delta} \tag{37}$$

In Equation (37), q'' represents the heat flux, λ is the thermal conductivity of stainless steel, Tw is the heating wall temperature in K, and Tm is the temperature at the steel contact interface, which remains at the melting point of 1700 K during contact melting. Substituting the heat flux and liquid film thickness from Figure 4 into this equation yields the wall temperature T_w, whose variation range is plotted on the *x*-axis of Figure 11. Consequently, the extremely small value of the film thickness means that even significant variations in heat flux result in only minimal changes in T_w. This explains the narrow temperature range observed in the figure.

Figure 11 illustrates the effect of heat source mass on melting velocity under the Dirichlet boundary condition. Unlike the case with the second-kind boundary condition, an increase in heat source mass enhances the melting velocity. This phenomenon is primarily attributed to the extremely small liquid film thickness, on the order of 10^{-6} m. As shown in Figure 5, an increase in mass leads to a reduction in the film thickness δ. According to Equation (37), a constant wall temperature, Tw, coupled with a decreasing δ, results in a significant increase in the heat flux q'', which consequently enhances the melting velocity U. Owing to the minimal value of δ, even a minor change in T_w is amplified into a substantial variation in q'', thereby inducing a pronounced response in U.

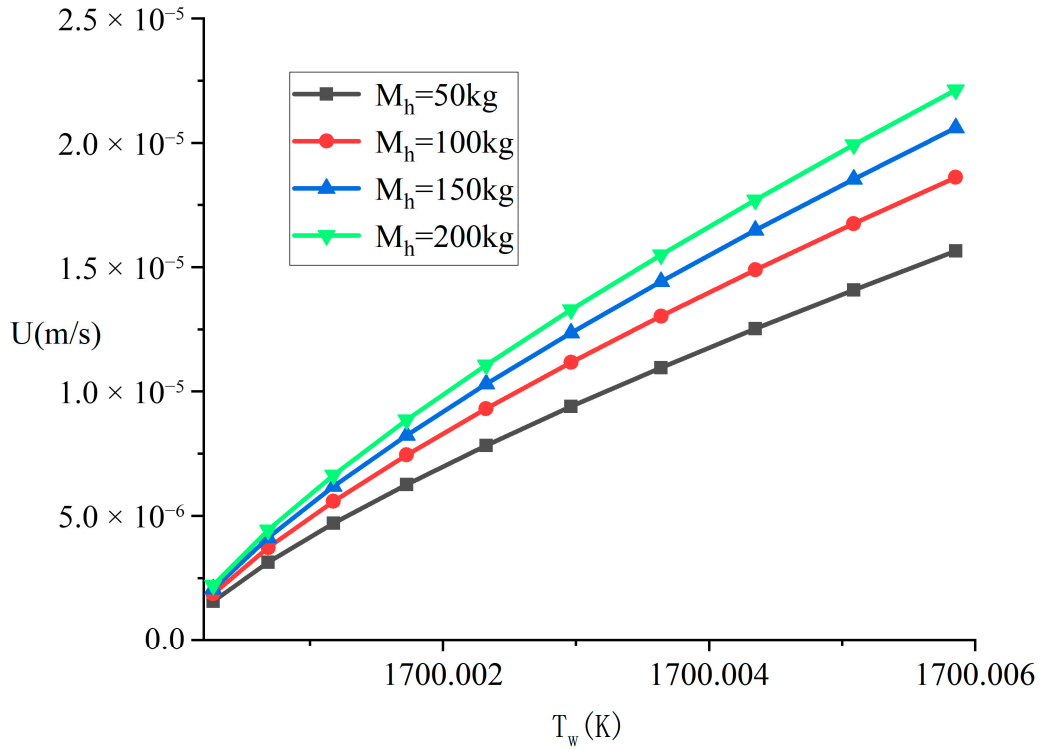


Figure 11. Effect of heat source mass on melting velocity under the Dirichlet boundary condition.

A comparative analysis of the governing equations for the two thermal boundary conditions—Equation (32) for the Neumann and Equation (36) for the Dirichlet—reveals that under the Neumann boundary condition, the melting velocity depends solely on the input heat flux q''. In contrast, under the first-kind boundary condition, the melting velocity is influenced by the heat source gravity and geometric parameters, as the heat flux magnitude under constant temperature conditions depends on the liquid film thickness. This coupling characteristic makes the melting velocity highly sensitive to parameters during numerical solving, easily triggering strong nonlinear effects, numerical oscillations, and convergence difficulties. Additionally, minor fluctuations in the temperature of the heater contact surface are challenging to capture and track dynamically. In summary, the contact melting governing equation under the Neumann boundary condition is more suitable for numerical coupling calculations.

5. Conclusions

Based on the theory of contact melting, this study developed a three-dimensional model for the contact melting of corium crust against stainless steel plates under severe accident conditions through reasonable assumptions and theoretical modeling. The validity of the model was demonstrated by comparisons with experimental results. Sensitivity analysis of model parameters and error assessment between two- and three-dimensional models revealed key factors influencing melting characteristics. Finally, by comparing the governing equations under Dirichlet and Neumann thermal boundary conditions, the most suitable type of governing equation for numerical modeling of severe reactor accidents was identified. The main conclusions are summarized as follows:

1. Under the Neumann boundary condition (constant heat flux), the melting velocity depends solely on the magnitude of the heat flux and the temperature gradient within the phase-change material itself, whereas the influence of the geometric dimensions of the contact surface and the weight of the heat source on the melting velocity is negligible.
2. Under the Neumann boundary condition (constant heat flux), an increase in heat source gravity and aspect ratio of the contact surface suppresses the liquid film thickness, thereby reducing the thermal resistance of the melting process and consequently accelerating melting. Conversely, an increase in heat flux and contact area promotes liquid film thickening. It is noteworthy that as heat source gravity and contact area continue to increase, their influence on the variation of liquid film thickness gradually diminishes. Furthermore, the effects of heat flux and aspect ratio on liquid film thickness are independent of each other, with no significant interactive effects observed.
3. The discrepancy in melting velocity calculations between the three-dimensional and two-dimensional models is negligible. However, significant errors arise in the calculation of liquid film thickness. When the aspect ratio of the contact surface exceeds six, the error between the three-dimensional and two-dimensional models remains below 4%. Therefore, for most internal reactor components characterized by narrow geometric features, the two-dimensional model can effectively simulate the melting process.
4. In the governing equations based on the Dirichlet thermal boundary condition, the melting velocity is influenced by the complex coupling of multiple factors such as geometric relationships and heat source mass. In contrast, under the Neumann thermal boundary condition, the melting velocity is directly controlled solely by the magnitude of the heat flux and the slope of the contact surface. This decoupling characteristic significantly reduces the computational complexity and potential instabilities introduced

by multi-factor coupling, thereby effectively enhancing the robustness and accuracy of the numerical solutions. Considering the power variation characteristics within reactors, the use of the governing equation under the second-kind boundary condition is recommended for severe accident scenarios.

The objective of this research is to establish a foundational understanding of the contact melting mechanism. To this end, the model simplifies material property variations and interfacial geometry, while effects like radiation heat transfer and chemical interactions are intentionally omitted. Exploring these aspects within a more complex and realistic core environment is identified as a critical avenue for future work.

Author Contributions: Conceptualization, W.C. and Y.C.; methodology, W.C.; validation, J.M.; data curation, J.M.; writing—original draft preparation, J.M.; writing—review and editing, W.C. and H.X.; visualization, J.M.; supervision, Y.C.; project administration, Y.C. All authors have read and agreed to the published version of the manuscript.

Funding: This research was financially supported by the National Natural Science Foundation of China (project number 12175311).

Data Availability Statement: The original contributions presented in this study are included in the article. Further inquiries can be directed to the corresponding author.

Conflicts of Interest: The authors declare no conflicts of interest to report regarding the present study.

Nomenclature

U	melting velocity, m/s	P	liquid film pressure, Pa
δ	liquid film thickness, m	α	thermal diffusivity, m^2/s
x, y, z	cartesian coordinates	λ	thermal conductivity, W/(m·K)
u, v, w	velocity in the x, y, and z directions, m/s	μ	dynamic viscosity, kg/(m·s)
c_p	specific heat capacity, J/(kg·K)	ρ	density, kg/m^3
a	contact surface length, m	M	mass, kg
b	contact surface width, m	ξ	aspect ratio
S_c	contact surface area, m^2	Subscripts	
L_m	latent heat, J/kg	m	for the melt
q''	heat flux, W/m^2	h	for the heater

References

1. Zhang, Y.P.; Niu, S.P.; Zhang, L.T.; Qiu, S.Z.; Su, G.H.; Tian, W.X. A review on anlysis of LWR severe accident. *J. Nucl. Eng. Rad. Sci.* **2015**, *1*, 041018. [CrossRef]
2. Jacquemain, D. *Nuclear Power Reactor Core Melt Accidents: Current State of Knowledge*; EDP Sciences: Paris, France, 2015.
3. Müller, W.C. Review of debris bed cooling in the TMI-2. *Nucl. Eng. Des.* **2006**, *236*, 1965–1975. [CrossRef]
4. Wang, X.; Cheng, X. Analysis of focusing effect of light metallic layer in stratified molten pool under IVR-ERVC condition. *J. Nucl. Eng. Rad. Sci.* **2015**, *1*, 021007. [CrossRef]
5. Liu, L.L.; Yu, H.X.; Chen, L.; Deng, J.; Zhang, H. A method for predicting configuration of corium pool in lower plenum of reactor vessel. *Nucl. Power Eng.* **2016**, *37*, 138–141. (In Chinese)
6. Luo, Y.J.; Liu, X.J.; Cheng, X. IVR-ERVC study of 1700MW class PWR based on MAAP simulation and coupled analysis. *Ann. Nucl. Energy* **2019**, *126*, 1–9. [CrossRef]
7. Ding, S.; Huang, H.F.; Zhong, R.H.; Zhang, X.Y.; Zhan, D.K. Numerical analysis of movement and heat transfer of melting material in PWR core. *At. Energy Sci. Technol.* **2020**, *54*, 44–52. (In Chinese)
8. Hou, L.Q.; Zhu, D.H.; Wu, Q.; Liu, Y.Z.; Liu, Z.D.; Zheng, H.T. Research of behavior of the core shroud and barrel during a severe accident. *Nucl. Sci. Eng.* **2020**, *40*, 827–835.
9. Moallemi, M.K.; Webb, B.W.; Viskanta, R. An experimental and analytical study of close-contact melting. *J. Heat Transf.* **1986**, *108*, 894–899. [CrossRef]
10. Chen, W.Z. *Analysis of Contact Melting*; Chinese Atomic Energy Press: Beijing, China, 2022.
11. Emerman, S.H.; Turcotte, D.L. Stoke's problem with melting. *Int. J. Heat Mass Transf.* **1983**, *26*, 1625–1630. [CrossRef]

12. Moallemi, M.K.; Viskanta, R. Analysis of melting around a moving heat source. *Int. J. Heat Mass Transf.* **1986**, *29*, 1271–1282. [CrossRef]
13. Chen, W.Z.; Hao, J.L.; Chen, Z.Y. A study of self-burial of a radioactive waste container by deep rock melting. *Sci. Technol. Nucl. Install.* **2013**, *2013*, 184757. [CrossRef]
14. Zhu, Y.X.; Zhang, Y.P.; Li, G.; Yang, F.J. Heat transfer processes during an unfixed solid phase change material melting outside a horizontal tube. *Int. J. Therm. Sci.* **2001**, *40*, 550–563. [CrossRef]
15. Oka, M.; Carey, V.P. A unified treatment of the direct contact melting processes in several geometric cases. *Int. Commun. Heat Mass Transf.* **1996**, *23*, 187–202. [CrossRef]
16. Mayer, P.; Moaveni, S. Close-contact melting as a subtractive machining process. *Int. J. Adv. Manuf. Technol.* **2008**, *37*, 980–995. [CrossRef]
17. Hu, Y.J.; Shi, M.H. Analysis of melt-film thickness profile in PCM solid close-contact melting around hot sphere. *Acta Energ. Sol. Sin.* **1998**, *19*, 23–27. (In Chinese)
18. Gong, M.; Chen, W.Z.; Zhu, B. Analysis of contact melting around a horizontal elliptical cylinder heat source. *Prog. Nat. Sci.* **2008**, *18*, 697–702. [CrossRef]
19. Ma, J.J.; Chen, W.Z.; Xiao, H.G. Study of contact melting of plate bundles by molten material in severe reactor accident. *Nucl. Eng. Technol.* **2023**, *55*, 4266–4273. [CrossRef]
20. OECD Nuclear Energy Agency. *Progress Made in the Last Fifteen Years Through Analyses of the TMI-2 Accident Performed in Member Countries*; OECD/NEA Report NEA/CSNI/R(2005)1; OECD: Paris, France, 2005.
21. Judd, M. *An Introduction to the Engineering of Fast Nuclear Reactors*; Cambridge University Press: New York, NY, USA, 2014.
22. Hong, H.; Saito, A. Numerical method for direct contact melting in transient process. *Int. J. Heat Mass Transf.* **1993**, *36*, 2093–2103. [CrossRef]
23. Fomin, S.A. Mathematical model of heat and mass transfer processes in contact melting. *J. Math. Sci.* **1992**, *61*, 2426–2438. [CrossRef]
24. Salamatin, A.N.; Fomin, S.A.; Chistyakov, V.K.; Chugunov, V.A. A mathematical description and calculation of contact melting. *J. Eng. Phys.* **1984**, *46*, 439–446. [CrossRef]
25. Courant, R.; Hilbert, D. *Methods of Mathematical Physics*; Wiley-VCH: Weinheim, Germany, 1989.
26. Yoo, H. Analytical solutions to the unsteady close-contact melting on a flat plate. *Int. J. Heat Mass Transf.* **2000**, *43*, 1457–1467. [CrossRef]
27. Schnitzler, B. *Fission Product Decay Heat Modeling for Disrupted Fuel Regions (FDECAY)*; Report EGG-NSRD-5475; EG&G Idaho, Inc.: Idaho Falls, ID, USA, 1981.
28. Moallemi, M.K.; Viskanta, R. Experiments on fluid flow induced by melting around a migrating heat source. *J. Fluid Mech.* **1985**, *157*, 35–51. [CrossRef]

Disclaimer/Publisher's Note: The statements, opinions and data contained in all publications are solely those of the individual author(s) and contributor(s) and not of MDPI and/or the editor(s). MDPI and/or the editor(s) disclaim responsibility for any injury to people or property resulting from any ideas, methods, instructions or products referred to in the content.